Regular Article – Experimental Physics

Excitation and γ -decay coincidence measurements at the GRAF beamline for studies of pygmy and giant dipole resonances*

N. Kobayashi^{1,a}, K. Miki², T. Hashimoto³, C. Iwamoto⁴, A. Tamii¹, N. Aoi¹, M.P. Carpenter⁵, K. Hatanaka¹, J. Isaak⁶, E. Ideguchi¹, S. Morinobu¹, S. Nakamura¹, and S. Noji⁷

- Research Center for Nuclear Physics, Osaka University, Ibaraki, Osaka 567-0047, Japan
- $^{2}\,$ Department of Physics, Tohoku University, Ao
ba, Sendai, Miyagi 980-8587, Japan
- ³ Rare Isotope Science Project, Institute for Basic Science, 70, Yuseong-daero, 1689-gil, Yuseong-gu, Daejeon, Korea
- Center for Nuclear Study, University of Tokyo, RIKEN Campus, Wako, Saitama 351-0198, Japan
- ⁵ Physics Division, Argonne National Laboratory, Argonne, IL 60439, USA
- ⁶ Institut für Kernphysik, Technische Universität Darmstadt, Schlossgartenstraße 9, D-64289 Darmstadt, Germany
- National Superconducting Cyclotron Laboratory, Michigan State University, East Lansing, MI 48824, USA

Received: 24 April 2019 / Revised: 24 July 2019

Published online: 2 December 2019

© Società Italiana di Fisica / Springer-Verlag GmbH Germany, part of Springer Nature, 2019 Communicated by N. Alamanos

Abstract. Physical studies of electric dipole excitations in atomic nuclei e.g. the structure of pygmy dipole resonances and isovector giant dipole resonances are attracting much attention recently. In this article, we describe a technical development in the coincidence measurement of the excitation processes with the Grand Raiden high-resolution magnetic spectrometer and the γ -decay processes by the CAGRA and SC γ LLA efficient γ -detector arrays at the Research Center for Nuclear Physics at Osaka University. Specifically, we describe how we developed a new beamline (GRAF), for γ detection at the target position by placing the spectrometer at an angle of 4.5–19.0° and by transporting the primary beam to a well-shielded beam dump. Experimental conditions and representative data are shown for each of the two γ -detector arrays.

1 Introduction

Electric dipole (E1) excitation is one of the fundamental excitation modes in atomic nuclei [1]. The IsoVector Giant Dipole Resonance (IVGDR), commonly observed in all nuclei which consist of protons and neutrons, is microscopically described as a collective, out-of-phase dipole oscillation of protons and neutrons. The IVGDR accounts for a major part of the energy weighted sum-rule (Thomas-Reiche-Kuhn (TRK) sum-rule) of the E1 reduced transition strength [2]. While the main strength is located at higher energies than the neutron separation energy (S_n) , another concentration of the strength has been found in the vicinity of S_n . This low-energy dipole strength is often called the Pygmy Dipole Resonance (PDR), which seems to commonly exist also in neutron-rich nuclei with a mass number greater than $A \sim 90$. The PDR accounts for only a few percent of the TRK sum-rule in stable nuclei. The dependence of this sum-rule fraction on the neutron excess has been predicted by several theoretical models [3] but

has not been clearly confirmed yet [4]. The properties of the E1 excitation mode, especially the origin of the PDR, is one of the main motivations for the present research on this issue.

The E1 response of nuclei has been widely studied by real-photon beam measurements [5]. However, in most of the measurements only the deexcitation γ rays were detected without tagging of the excitation energy. Consequently, the observed γ rays which were creating a photopeak were analyzed as if they were single γ transitions from the initial excited state to the ground state (g.s.). The analysis implicitly assumed a 100% branching ratio of the g.s. γ -decay channel. Although it is often the dominant decay channel below S_n , this assumption is in general invalid. In fact, monochromatic real-photon experiments and statistical-decay models showed g.s. γ -decay branching ratios of 80 to 50% [4] depending on the excitation energy, and in some cases, much smaller than that [6]. The observation unavoidably depends on the experimental sensitivity to the weak transitions and to the high level density, and thus the attained values should be carefully treated. For a full understanding of this fundamental excitation mode, it is important to measure both excitation and decay processes simultaneously.

^{*} Contribution to the Topical Issue "Giant, Pygmy, Pairing Resonances and Related Topics" edited by Nicolas Alamanos, Ricardo A. Broglia, Enrico Vigezzi.

a e-mail: kobayash@rcnp.osaka-u.ac.jp

An experimental technique has been developed [7,8] based on proton-scattering measurements at relativistic energy and at extremely forward angles using the Grand Raiden (GR) [9] high-resolution spectrometer at the cyclotron facility of the Research Center for Nuclear Physics (RCNP) at Osaka University. The E1 response as well as the spin-M1 response of stable nuclei has been extracted, fully covering the PDR and GDR excitation energies in the vicinity of S_n with high resolution, good statistical accuracy, and a high sensitivity to weak excitations. The experimental method utilizes the dominance of the Coulomb excitation in the cross section of the proton scattering at very forward angles. The excitation process is probed without any dependence on the active decay channel. Quite a few significant results on nuclear structure achieved using this method are summarized in a recent review paper [8]. The purpose of this article is to describe an extension of this experimental approach to γ -decay coincidence measurements.

Amongst the decay channels, γ decay has the simplest dynamics since the mediating electromagnetic interaction is known precisely and its transition rate gives nuclear-structure information for the same nuclide. In contrast, particle-decay processes are affected by the penetrability of the particle through the potential barrier or the distortion of the wave function in the nucleus. The transition is relevant to the coupling between the parent and the daughter, which makes the theoretical interpretation more complex. Thus, we focus on the γ decays in this paper.

Coincidence measurements between the excitation and γ -decay processes provide a lot of additional information on the nuclear excited states. First, with the coincidence measurement, the branching ratio of the populated excited state to the detected decay channel is directly observable. The branching ratio is defined as the ratio of the transition rate of the specified decay channel (partial decay width) to the sum of the transition rates of all the decay channels (total decay width). The latter also includes the spreading rate of the initially populated component (doorway) of the excited state into more complex components. The branching ratios are obtained either for each excited state (provided that the state is well-separated from the other states compared to the experimental resolution), or for many states contained in each excitation energy bin, as an averaged value. For the ground-state γ decay especially, the decay-transition rate is equivalent to the Coulomb excitation transition rate with a trivial spin factor, by the detailed balance principle [2]. This provides us with a unique way to study the total decay width of the excited states including collective giant resonances. Second, the branching ratios among different γ -decay channels provide the relative strength due to the coupling of the excited state to each daughter state populated by the initial γ decay. Further insights into the internal structure of the excited state can be obtained from the information on relative strengths [10]. Third, the spatial distribution of the emitted γ -rays, or more precisely, the angular correlation between the γ -ray and the scattered particle, has a specific intensity distribution depending on the spin-parity of the parent excited state and the daughter state. This

information is useful for the spin-parity assignments of isolated states and for the multipole decomposition of mixed multiple states. Fourth, experimentally, the use of γ -ray detectors often allows for the precise measurement of the γ -ray energies. Using this data, better resolution can be achieved in determining the excitation energy of the individual state than is possible with a momentum analysis of the scattered particle alone. Also, since the E1 transition dominates in the γ -decay process, the γ -coincidence itself enhances the detection of the corresponding spin-parity of the excited states.

 γ -decay measurement is often limited to excitation energies below S_n because the neutron decay becomes dominant once its decay channel is open. Nevertheless, γ -decay measurements at energies above S_n are becoming much more feasible after pioneering work [11] in the IVGDR region. Such measurements will certainly provide unique information on the decay mechanism of giant resonances which has never been accessible using other methods.

For the excitation part of the measurement, a combination of the beam and the detected scattered particles is selected for the relevant excitation mode in each study. For example, proton inelastic scattering has selectivity for E1 and spin-M1 excitations at very forward angles [8]. Alphaparticle inelastic scattering is useful for probing isoscalar excitations [12] as well as for studying the isospin nature of the PDR [4,5]. The charge-exchange (3 He, t) reaction is excellent for the study of Gamow-Teller excitations at very forward angles [13–16]. In this article, we will deal with proton and alpha inelastic scatterings.

For the realization of the γ -decay coincidence measurement, it is essential to stop the primary beam in a well-shielded beam dump that is located sufficiently far from the target position since the γ -detectors surrounding the target are usually sensitive to background radiation from the beam stopper. At the RCNP cyclotron facility, a 0° inelastic-scattering setup in the transmission mode provides one feasible method. In this case, the GR spectrometer is placed at 0° and the beam that passes through the target is transported inside the spectrometer and is stopped at a beam-dump downstream of the focal plane. Further details on this experimental technique are described in refs. [7,8]. For accommodating forwardmode particle scattering at angles larger than 4.5°, a new beamline, named the Grand RAiden Forward mode (GRAF) beamline, has been newly constructed. The unreacted beam after the target is deflected and separated from a central orbit of the GR spectrometer, and is transported to a beam dump located in a shield wall about 25 m downstream. More details about the GRAF beamline are described in sect. 2 of this article. The GRAF beamline was constructed for this kind of coincidence measurement as well as for particle scattering measurements with highly intense beams.

After a few pioneering measurements of γ -decay coincidence with the GR spectrometer using NaI detectors [17, 18], a series of experiments were performed using the Clover Array Gamma-ray spectrometer at RCNP/RIBF for Advanced research (CAGRA) [19]. In addition to the twelve CAGRA detectors, four large volume LaBr₃:Ce

scintillators were installed at the target position of the GR spectrometer. Proton, alpha, and ⁶Li scattering experiments were carried out using either the 0° inelasticscattering mode or the GRAF mode. While the germanium detectors have excellent energy resolution for γ rays, their detection efficiency is low at energies above a few MeV. Additionally, they are susceptible to neutron radiation damage. Following the CAGRA experiments, a pilot experiment was performed to measure the coincidence of γ decay of giant resonances to the g.s. This experiment utilized a newly constructed $SC\gamma LLA$ (Supporting Construction for γ -ray-detecting Large LaBr₃ Array) consisting of large volume LaBr₃:Ce scintillators [20]. LaBr₃:Ce detectors have much higher detection efficiency, timing resolution, and rate capability as compared to germanium detectors and they have better energy resolution than NaI(Tl) scintillators, which provides a great opportunity to study rare γ decays at excitation energies up to a few 10 MeV. In this article, we present a few examples from the γ -coincidence experiments where CAGRA and $SC\gamma LLA$ were coupled with the GR spectrometer.

This manuscript is organized as follows: In sect. 2, the GRAF beamline and the GRAF mode are described as well as the other three modes of the beamline and the spectrometer. The technical information, the ion optics, and the commissioning results of the GRAF beamline are reported. Section 3 explains the campaign experiments performed using the CAGRA, GR spectrometer, and the GRAF beamline. Section 4 discusses a pilot γ -coincidence measurement with SC γ LLA coupled with the GR spectrometer. Finally, the summary and outlook are given in sect. 5.

2 GRAF beamline

The GRAF beamline, constructed in 2014 at the West Experimental Hall of the RING Cyclotron Facility at RCNP, transports the unreacted beam from the target to a well-shielded wall beam dump located 25-meters downstream from the target. The purposes of the GRAF beamline were a) to couple several types of detectors surrounding the target to the GR spectrometer, and b) to measure angular distributions at forward angles using the GR spectrometer with an intense beam of up to $1\,\mu\mathrm{A}$. An example of a), using plastic detectors for the detection of protons, is published in ref. [21]. An example of b) is reported in ref. [22].

The GRAF beamline was added to the existing three modes of the beam transport: the 0° inelastic-scattering mode, the 0° charge-exchange- or transfer-reaction mode, and the WS-Long mode. Table 1 summarizes the four modes. In the following section, the GRAF beamline is described in detail, after briefly introducing the other three modes.

The 0° inelastic-scattering mode is used in inelastic-scattering measurements at forward angles of $0-3^{\circ}$ within the vertical angular acceptance of the GR spectrome-

ter. The GR spectrometer has an angular acceptance of $\pm 20\,\mathrm{mrad}$ in the horizontal direction and $\pm 50\,\mathrm{mrad}$ in the vertical direction. The GR spectrometer is centred at 0°. The unreacted beam is transported through the GR spectrometer together with the scattered particles and is stopped by a Faraday cup at a 0° dump [7,8]. The maximum beam intensity is limited by radiation safety requirement and is $\sim 10\,\mathrm{nA}$, depending on the beam particle and energy.

The 0° charge-exchange- or transfer-reaction mode is used to measure reactions where the particle to be detected is different than that of the beam. The GR spectrometer is also centred at 0° in this mode. The unreacted beam is stopped by a Faraday cup at the first dipole magnet of the GR spectrometer (GR-D1). The maximum beam intensity is 10–100 nA, depending on the beam particle and energy. The Large Acceptance Spectrometer (LAS) [23] can be placed between 61° and 120° in both 0° inelastic-scattering and 0° charge-exchange- or transfer-reaction modes.

The WS-Long mode is used to measure inelastic scattering at large angles. The GR spectrometer can be set at 25.5-70.0° in this mode, and owing to the horizontal angular acceptance of the GR spectrometer, the scattering angle range from 24.5° to 71.0° can be covered. The unreacted beam is guided to the wall beam dump by the WS-Long beamline. This beamline follows a straight line at an angle of 0°, and features a quadrupole doublet QM11U/D and a quadrupole triplet QM12U/M/D. These magnets are also used in the GRAF beamline, as shown in fig. 1, wherein the position of the QM11U/D doublet is changed. The maximum beam intensity of the WS-Long mode is around $1 \mu A$. The angular spread of 99% of the beam on the target should be smaller than the angular acceptance at the entrance of part QM11U/D, i.e., about 13 mrad, for good transmission of the beam from the target position to the wall beam dump. The LAS can be oriented from 25.5° to 120°. This mode has been used to perform coincidence measurements with the GR and the LAS [24].

The GRAF mode is a newly-developed mode in which the GRAF beamline is used. A topview of the beamline is shown in fig. 1. The GR spectrometer can be oriented from 4.5° to 19.0° with the exception of angles from 11.5° and 12.5° as the unreacted beam would hit a support bar in the vacuum chamber shown in the inset of fig. 1. Owing to the horizontal angular acceptance of the GR spectrometer, a scattering angle range from 3.5° to 20.0° can be covered. The ion optics of the GRAF beamline are optimized depending on the ratio of magnetic rigidity of the GR spectrometer $(B\rho_{\rm GR})$ to that of the beam $(B\rho_{\text{Beam}})$, $R_{B\rho} = B\rho_{\text{GR}}/B\rho_{\text{Beam}}$. For instance, for inelastic-scattering and the (³He, t) reaction, these ratios are well suited for $R_{B\rho} = 1$ and $R_{B\rho} = 2$, respectively. For reactions with $R_{B\rho}$ below 1 or above 2, the most-forward angle is larger than 4.5°. In addition, the angular spread of the beam on the target should be smaller than approximately 5 mrad for 99% of the beam, to achieve good beam transmission. The LAS can be oriented from 61° to 120°.

Mode	Beam stopper	Max. beam	GR angle	LAS angle
		intensity	(Coverage)	(Coverage)
0° inelastic-	0° dump	$\sim 10\mathrm{nA}$	0°	61–120°
scattering			$(0-\sim3^\circ)$	$(58 – 123^{\circ})$
0° charge-exchange-	Faraday cup	$10 – 100 \mathrm{nA}$	0	61120°
or transfer-reaction	in GR-D1		$(0-\sim3^\circ)$	$(58 – 123^{\circ})$
GRAF	Wall beam dump	$\sim 1 \mu \mathrm{A}$	$4.511.5^{\circ}$ and $12.519.0^{\circ}$	61120°
			$(3.5 - \sim 20.0^{\circ})$	$(58 – 123^{\circ})$
WS-Long	Wall beam dump	$\sim 1\mu\mathrm{A}$	$25.5 – 70.0^{\circ}$	25.5120°
			$(24.5 - \sim 71.0^{\circ})$	$(22.5-123^{\circ})$

Table 1. Summary of the modes of beam transportation.

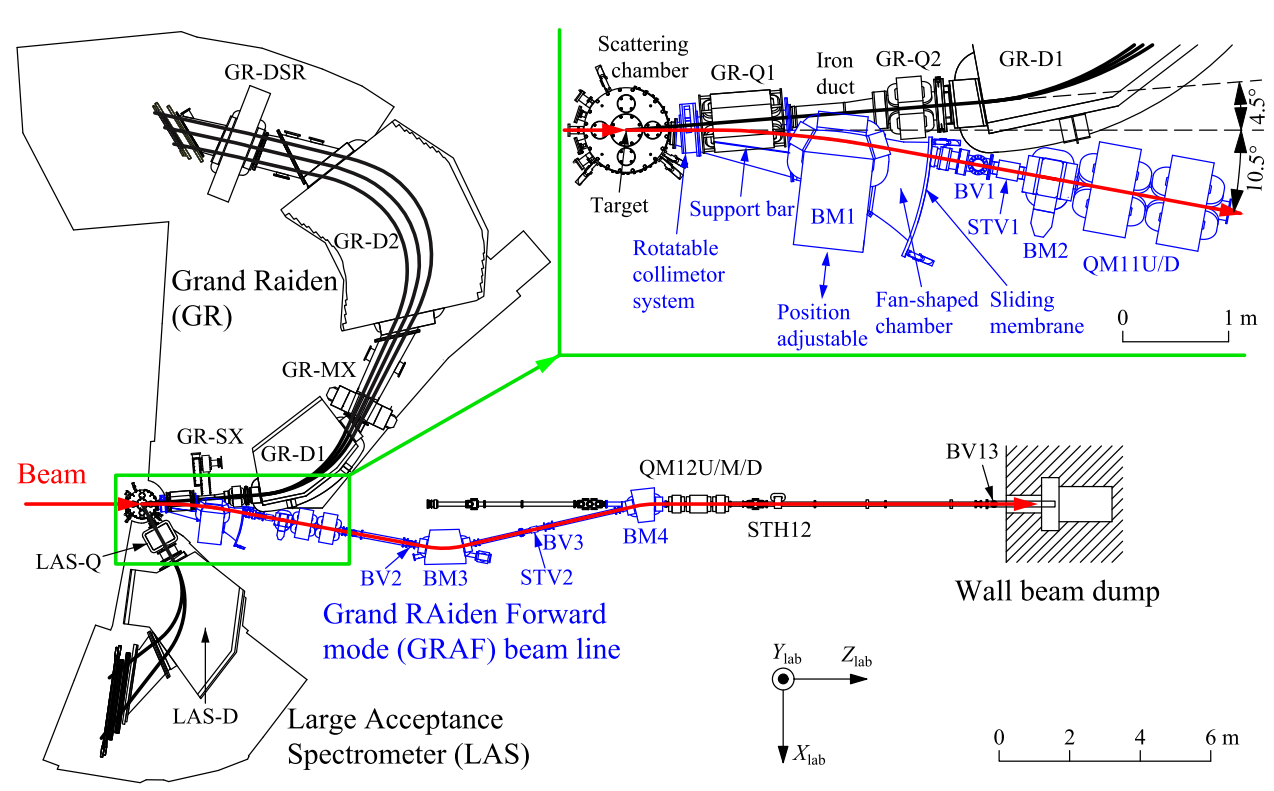
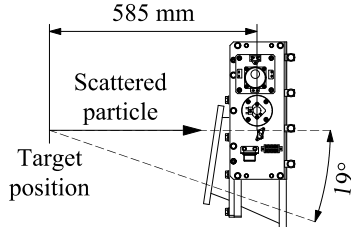


Fig. 1. The top view of the GRAF beamline, the GR spectrometer, and the LAS are shown. The inset represents a zoomed view of the GRAF beamline around the target. The GR angle is set to 4.5° , and the LAS angle is set to 61° . Also, the directions of the laboratory coordinate system (X_{lab} , Y_{lab} , Z_{lab}) are shown.

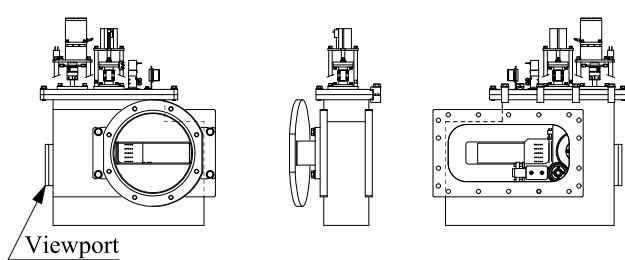
In the construction of the GRAF beamline, a scattering chamber called the GRAF scattering chamber, a collimator system, the GR-Q1 chamber, the iron vacuum duct between GR-Q1 and GR-Q2, the fan-shaped chamber, dipole magnets (BM1, BM2, BM3, and BM4), beam viewers (BV1, BV2, and BV3), and vertical steerers (STV1 and STV2) were manufactured. The GRAF scattering chamber was designed to fit to the GRAF mode. On the other hand, if the GRAF beamline is removed, the chamber will cover angles of the GR spectrometer from -1° to 70° . The structure of the sliding membrane is the same as that of the former scattering chamber. In a reference measurement, a collimator is placed downstream of the target in order to define the angular acceptance of the GR spectrometer. The collimator system was developed to allow for the remote selection of one of the pre-installed colli-

mators without breaking the vacuum. Figure 2 shows a) the top view of the system, b) the side view of the collimator box, and c) the side view of the system. The system has four slots to insert different collimators. These collimators can be changed using the stepping motor via the PLC controller. The GR-Q1 chamber was designed so that both the scattered particles and the beam can pass through the chamber at the GR angle (θ_s) of 4.5 to 19°. The vertical and horizontal gaps of the chamber are $160 \,\mathrm{mm}$ and $\sim 130 \,\mathrm{mm}$, respectively, in the region of the scattered particles, while the vertical gap is 28 mm in the region of the beam. The iron duct between the GR-Q1 and GR-Q2 replaces the GR-SX and the GR-Q1 Faraday cup (Q1-FC) when the GRAF mode is in operation. The duct is made of iron to shield the fringing magnetic field of the BM1 from the scattered particles which pass through the

a) Topview of the collimator system



b) Sideview of the chamber



c) Sideview of the collimator system

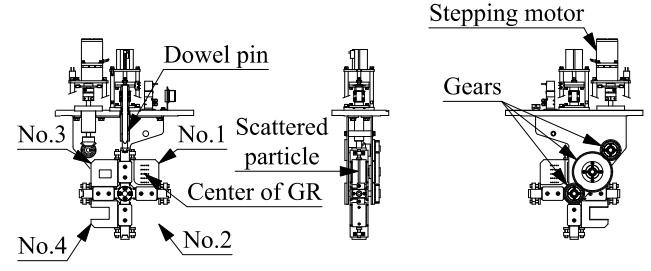


Fig. 2. (a) A top view of the collimator system, (b) a side view of the collimator box, and (c) a side view of the system are shown. The collimators are pre-installed at the slot nos. 1–4, respectively. The position of the collimator is defined by the dowel pin with an accuracy of $\sim 0.1\,\mathrm{mm}$. The distance between the target and the centre of the collimator was designed to be 585 mm.

GR spectrometer. The design of the beam viewers BV1, BV2, and BV3 are the same as the viewers used in other beamlines at RCNP. The fan-shaped chamber has a vertical gap of 52 mm at the BM1 and 70 mm at the exit of the chamber. The chamber has a sliding membrane between the BM1 and BV1 as indicated in fig. 1. Hence, the GR spectrometer can be rotated to any angle between 4.5° and 19.0° without venting the beamline. The specifications of the dipole magnets and the quadrupole magnets are summarized in tables 2 and 3, respectively. The BM1 magnet is placed on linear guides, because the position of the BM1 needs to be adjusted depending on θ_s and $R_{B\rho}$. A stepping motor can horizontally drive the BM1 along its vertical symmetry plane. The actual positions of the BM1 for each set of θ_s and $R_{B\rho}$ are listed in table 4. The BM1 position used in the case of $\theta_s = 4.5^{\circ}$ and $R_{B\rho} = 1$ is defined as the origin. The positive value of the position corresponds to the insertion facing towards the GR spectrometer. The steerers STV1 and STV2 are used if the central orbit of the beam needs to be tuned in the vertical direction. If all the components are perfectly aligned, these steerers are not necessary.

Table 2. Specifications of the dipole magnets BM1, BM2, BM3, and BM4 are shown. The positive sign of the bending angle corresponds to right-hand side deflection, and that of the edge angle corresponds to horizontal defocusing.

			_	
Specification	BM1	BM2	BM3	BM4
Magnet gap, g (mm)	70	120	70	70
Bending Radius (mm)	2,500	4,587	2,500	2,500
Bending angle	13°	-2.5°	-23.5°	13°
Edge angle at entrance	30°	2.5°	0°	0°
Edge angle at exit	30°	0°	0°	0°
Max. field strength (T)	1.3	0.7	1.3	1.3
Number of turns, N	280	400	512	512
Max. current (A)	316	181.5	158.2	156.3

In addition to manufacturing new devices, modifications were made to the sextupole magnet of the GR spectrometer (GR-SX), along with GR-Q1, Q1-FC, and GR-Q2. GR-SX and Q1-FC would inhibit the BM1 and the fan-shaped chamber of the GRAF beamline and thus these are placed on linear guides and removed from the beamline when in GRAF mode operation. A larger chamber for Q1-FC was fabricated so that it fits with the new GR-Q1 chamber and covers the angles $\theta_s=4.5$ to 19°. The side return yoke of GR-Q1 was cut so that the beam could pass through the gap between the poles of GR-Q1. The position of the GR-Q2 was moved downstream by 149 mm and the side return yoke of GR-Q2 was cut off to avoid encroaching on the fan-shaped chamber.

2.1 Ion optics

The ion optics of the GRAF beamline allow the unreacted beam to be transported to the beam dump when the GR spectrometer is oriented at $\theta_s=4.5\text{--}19.0^\circ.$ The main idea of the ion-optical design is to utilize the bending power of the GR-Q1 magnet and BM1 to remove the unreacted beam from the central orbit of the GR spectrometer. The unreacted beam is guided by BM1 and BM2 so that its orbit is centred on the axis of the QM11U/D magnets. The beam is doubly focused at BV3 and BV13 by the QM11U/D and QM12U/M/D magnets, and eventually stopped by the Faraday cup in the wall beam dump.

Two coordinate systems are used in this section for the description of the ion optics of the GRAF beamline. The laboratory coordinate system $(X_{\text{lab}}, Y_{\text{lab}}, Z_{\text{lab}})$ shown in fig. 1 is used to describe the trajectory of the beam in the West Experimental Hall, and the origin is fixed at the target position. The Y_{lab} direction is vertically up with respect to ground. The Z_{lab} direction is the direction of the central orbit of the beam towards the target. The X_{lab} axis is defined by the Y_{lab} and Z_{lab} axes in accordance with the left-handed coordinates that were used in the ion-optical design. It is noted that the right-handed coordinate is usually adopted in the standard analysis of experimental data used at RCNP. The beam-centre coordinate system (x, y, z) is to show the spatial shape of the beam, and

Specification	$\mathrm{QM11U/D}$	$\mathrm{QM}12\mathrm{U/D}$	QM12M
Product type	large aperture A	L_2	S_3
Aperture (mm)	115	106	106
Pole length (mm)	400	250	500
Number of turns per pole	318	160	160
Maximum current (A)	75	92	92
Maximum field gradient (T/m)	13	11	11

Table 3. Specifications of the quadrupole magnets QM11U/D and QM12U/M/D are shown.

Table 4. The beam position (X_{lab}) and angle $(\tan^{-1}(dX_{lab}/dZ_{lab}))$ at $Z_{lab} = 1.5$ m are shown for each set of θ_s and $R_{B\rho}$ as well as the transfer matrix elements between the target and the position at $Z_{lab} = 1.5$ m. These results are obtained from the beam trajectories calculated using Opera-3D TOSCA. The position of BM1 is shown for each parameter set.

			$R_{B\rho} = 1$				
GR angle θ_s	$> 19.0^{\circ}$	4.5°	7.0°	10.0°	4.5°	7.0°	10.0°
$X_{\mathrm{lab}} \; (\mathrm{mm})$	0.0	40.2	31.1	11.3	77.0	58.0	21.9
$\tan^{-1}(dX_{\text{lab}}/dZ_{\text{lab}})$ (deg.)	0.0	5.7	3.6	1.2	10.2	6.5	2.3
Position of BM1 (mm)	100.0	0.0	35.0	100.0	-20.3	14.2	68.0
Transfer matrices							
(x x)	1.000	1.194	0.533	0.743	1.186	0.157	0.528
$(x \theta)$ (m/rad)	1.500	1.641	1.025	1.267	1.577	0.650	1.062
$(x \delta)$ (m)	0.000	-0.038	-0.029	-0.011	-0.069	-0.050	-0.020
(θx) (rad/m)	0.000	-0.076	-1.012	-0.472	-0.580	-1.713	-0.862
$(\theta \theta)$	1.000	0.699	-0.100	0.522	0.054	-0.833	0.133
$(\theta \delta)$ (rad)	0.000	-0.089	-0.055	-0.020	-0.137	-0.088	-0.036
(y y)	1.000	0.778	1.507	1.260	0.672	1.990	1.517
$(y \varphi)$ (m/rad)	1.500	1.334	1.991	1.722	1.310	2.456	1.960
$(\varphi y) \text{ (rad/m)}$	0.000	-0.111	1.197	0.525	-0.071	2.265	1.029
(arphi arphi)	1.000	1.094	2.238	1.501	1.374	3.304	1.985

the origin is located at a point at the central orbit of the beam. The z direction is defined as the beam direction. The directions of x and y are defined in the same way as in the $(X_{\text{lab}}, Y_{\text{lab}}, Z_{\text{lab}})$ coordinate system.

The unreacted beam passes through the gap between the poles of the GR-Q1 when the angle of the GR spectrometer is smaller than $\sim 14^{\circ}$. In this case, the beam is deflected to the right-hand side, and is focused in the x direction and defocused in the y direction, respectively, near the smallest gap of the poles of GR-Q1. The ratio between focusing and defocusing effects depends on θ_s and the strength of the magnetic field of GR-Q1, thus the beam transport after GR-Q1 should be re-tuned for each set of θ_s and $R_{B\rho}$. The beam trajectories for the GR-Q1 magnet were calculated numerically via the finite element method using Opera-3D TOSCA. The position X_{lab} and angle $\tan^{-1}(dX_{\rm lab}/dZ_{\rm lab})$ of the beam at $Z_{\rm lab}=1.5$ m are shown in table 4 for $\theta_s=4.5^\circ,7.0^\circ,10.0^\circ,$ and 19.0° and for each variant of $R_{B\rho}=1$ and 2. The trajectories at the GR-Q1 magnet were calculated for different initial conditions and for each set of θ_s and $R_{B\rho}$, determining transfer matrices at $Z_{\text{lab}} = 1.5 \,\text{m}$ as shown in table 4.

The beam transport from the target to the wall beam dump was designed by using the ORBIT program and the results are shown in table 4. The important point in the optimization of the ion-optical design is to reduce the beam size after the BM1 magnet to achieve good transmission. Therefore, if the beam size is large in the x direction at the entrance of the BM2 magnet, the beam needs to be focused horizontally by QM11U and needs to be vertically defocused by QM11D. The excitation currents for QM11U/D should be adjusted by measuring the beam spot size at the BV3 viewer to achieve double focusing in the x and y directions. After the BV3 viewer, the QM12U/M/D is tuned to achieve double focusing at the BV13 viewer. If the beam is doubly focused independently of θ_s and $R_{B\rho}$, the excitation configuration of the quadrupole triplet QM12U/M/D has two options, the horizontally focusing-defocusing-focusing configuration and the defocusing-focusing-focusing configuration for the U-M-D magnets. The configuration is selected using the transport calculations to reduce the beam size in the QM12U/M/D magnets. The optimal excitation currents of the magnets are summarized in table 5.

The envelope of the beam is calculated for the initial conditions, $x_0 = y_0 = \pm 0.5 \,\mathrm{mm}$, $\theta_0 = \varphi_0 = \pm 5 \,\mathrm{mrad}$, and a 2.5π -mm· mrad upright emittance ellipse in the x and y directions. Figure 3 shows the envelope for $\theta_s = 19^\circ$. In this case, the beam is not affected by GR-Q1, because the beam passes outside of GR-Q1. The beam is horizontally defocused due to the edge angle of BM1, and thus the beam size becomes large in the x direction at the entrance of BM2. Therefore, QM11U/D is operated in the horizontal focusing-defocusing configuration for the U-D magnets.

Table 5. The optimized excitation value of each magnet is shown for each set of θ_s and $R_{B\rho}$. The actual magnetic field of the dipole magnets or the magnetic gradient of the quadrupole magnets is the product of $B\rho_{\text{Beam}}$ and the listed values in the table. The positive sign corresponds to right-hand side deflection in a dipole magnet and horizontal defocusing in a quadrupole magnet, respectively.

			$R_{B\rho} = 1$		$R_{B\rho}=2$				
GR angle θ_s	$> 19.0^{\circ}$	4.5°	7.0°	10.0°	4.5°	7.0°	10.0°		
$1/\rho \text{ of BM1 (m}^{-1})$	0.400	0.148	0.237	0.334	-0.063	0.097	0.291		
$1/\rho \text{ of BM2 (m}^{-1})$	-0.218	0.013	-0.058	-0.163	0.205	0.073	-0.113		
$k_Q/B\rho_{\mathrm{Beam}}$ of QM11U (m ⁻²)	2.121	2.017	-1.949	2.085	-1.998	-2.192	-1.898		
$k_Q/B\rho_{\mathrm{Beam}}$ of QM11D (m ⁻²)	-1.886	-1.971	1.677	-1.953	1.625	2.072	1.782		
$1/\rho \text{ of BM3 (m}^{-1})$	-0.400	-0.400	-0.400	-0.400	-0.400	-0.400	-0.400		
$1/\rho \text{ of BM4 (m}^{-1})$	0.400	0.400	0.400	0.400	0.400	0.400	0.400		
$k_Q/B\rho_{\mathrm{Beam}}$ of QM12U (m ⁻²)	2.417	-2.519	-2.519	-2.519	-2.519	-2.519	2.417		
$k_Q/B\rho_{\mathrm{Beam}}$ of QM12M (m ⁻²)	-2.445	2.453	2.453	2.453	2.453	2.453	-2.445		
$k_Q/B\rho_{\mathrm{Beam}}$ of QM12D (m ⁻²)	2.417	-2.519	-2.519	-2.519	-2.519	-2.519	2.417		

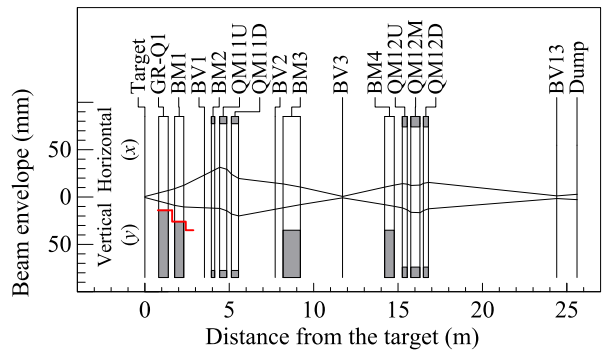


Fig. 3. The envelopes of the beam in the horizontal (x) and in the vertical (y) direction are shown for a GR angle of 19° . The red lines show the vertical aperture of the vacuum chamber. See the text for the initial conditions.

Figure 4 shows the envelopes for $R_{B\rho} = 1$ for angles of $\theta_s = 4.5^{\circ}$, 7.0° , and 10.0° . In the case of 7.0° , the vertical defocusing effect of GR-Q1 is the most prominent, and the beam becomes almost parallel in the x direction and is defocused in the y direction. For other angles, the beam is defocused in the x and y directions. Therefore, the QM11U/D doublet should be operated in the horizontal defocusing-focusing configuration. In the other cases, the opposite configuration, i.e., the horizontal focusingdefocusing configuration, is selected, which is the same as for $\theta_s = 19^{\circ}$. It is noted that, if the horizontal defocusingfocusing configuration is selected for angles other than 7.0°, the excitation configuration of QM12U/M/D may be changed in order to reduce the beam width. At other angles than 4.5° , 7.0° , and 10.0° , the excitation configuration of the QM11U/D and QM12U/M/D can be chosen by looking at the viewer BV1. If the beam width in the y direction is larger than in the x direction, then the excitation configuration of 7.0° is chosen.

Figure 5 shows the envelopes for $R_{B\rho}=2$ and $\theta_s=4.5^\circ,~7.0^\circ,~$ and $10.0^\circ.$ In this case, the effect of GR-Q1 is stronger than for $R_{B\rho}=1$, and the vertical beam size becomes large at the entrance of BM2. Therefore, QM11U/D should be operated in the horizontal defocusing-focusing

configuration, which is opposite to the case for $\theta_s=19^\circ$. The beam is focused in the x direction and strongly defocused in the y direction at $\theta_s=7.0^\circ$. The vertical beam size is rather large at BM1 for $\theta_s=7.0^\circ$. At $\theta_s=4.5^\circ$, the beam becomes almost parallel in the x direction and is defocused in the y direction. As a result, tuning to get good transport of the beam for this angle is difficult. The excitation configuration of QM12U/M/D is selected to balance the beam widths in the x and y directions.

2.2 Commissioning of the GRAF beamline

The commissioning of the GRAF beamline was performed in July 2014. The goals of the commissioning were a) to verify that all the components of the GRAF beamline were working within the design specifications, b) to establish proper operation of the ion optics, and c) to adjust the beam transport to minimize transmission losses, thereby optimizing the experimental conditions.

The ion optics was investigated for each parameter set of $R_{B\rho}=1$ and 2 and $\theta_s=4.5^\circ,~7.0^\circ,~$ and 19.0°. A proton beam at 65 MeV was used and scattered protons and deuterons were measured for $R_{B\rho}=1$ and 2, respectively. Two targets, one of ¹⁹⁷Au with an areal density of $1.68\,\mathrm{mg/cm^2}$ and one of ²⁰⁸Pb with an areal density of $5.2\,\mathrm{mg/cm^2}$ along with a blank target were used to measure the transmission. The angular spread of the beam caused by Coulomb multiple scattering at the target was calculated as $4.95\,\mathrm{mrad}$ for the ¹⁹⁷Au target and $9.57\,\mathrm{mrad}$ for the ²⁰⁸Pb target for 3σ .

The excitation current of each magnet was optimized with the blank target to maximize the beam transmission through the GRAF beamline by monitoring the beam size with the beam viewers. Table 6 compares the excitation currents predicted by ion-optical calculations (Cal.) and those optimized experimentally (Exp.). The magnetic field B of the dipole magnet is calculated by assuming the simple linear equation

$$B \simeq \frac{\mu_0}{g} NI,\tag{1}$$

Table 6. The optimal excitation current of each magnet is shown for each set of θ_s and $R_{B\rho}$. The positive sign of each value results in right-hand side deflection for the dipole magnet and horizontal defocusing for the quadrupole magnet, respectively.

				R_B	$\rho = 1$		$R_{B\rho}=2$				
GR angle θ_s	19.0°		4.	4.5°		7.0°		5°	7.0°		
	cal.	exp.	cal.	exp.	cal.	exp.	cal.	exp.	cal.	exp.	
Current (A)											
BM1	-94.30	-97.96	-35.00	-33.11	-55.88	-56.45	14.73	16.23	-22.85	-21.80	
BM2	-61.67	-55.15	4.04	5.06	-16.42	-11.86	58.00	59.41	20.79	21.77	
QM11U	10.49	10.37	9.98	9.07	-9.65	-9.37	-9.89	-8.59	-10.84	-10.70	
QM11D	-9.34	-8.54	-9.76	-9.22	8.31	8.21	8.05	5.67	10.26	10.16	
BM3	51.57	49.50	51.57	50.52	51.57	50.83	51.57	51.46	51.57	51.55	
BM4	51.57	49.53	51.57	50.76	51.57	50.37	51.57	50.76	51.57	50.50	
QM12U	20.45	20.12	-21.33	20.12	-21.33	-20.24	-21.33	-19.60	-21.33	-19.93	
QM12M	-20.69	-20.76	20.76	-20.76	20.76	19.31	20.76	19.08	20.76	19.51	
QM12D	20.45	20.12	-21.33	20.12	-21.33	-20.24	-21.33	-19.60	-21.33	-19.93	

Table 7. Transmission of the GRAF beamline is shown for each setting and target.

				$R_{B\rho} = 1$					$_{0}=2$
GR angle θ_s	19	.0°	4.	5°	7.0°			7.0°	
Target	blank	¹⁹⁷ Au	blank	blank ¹⁹⁷ Au		²⁰⁸ Pb	bla	nk	²⁰⁸ Pb
BS3 (nA)	4.3	5.0	3.2	4.7	12.0	12.7	12.	6	12.0
Wall dump (nA)	4.0	4.5	2.9	4.3	11.5	11.0	11.	7	9.8
Transmission	93%	90%	91%	92%	96%	87%	936	%	82%

where μ_0 , g, N, and I represent the permeability of free space, the gap size, the number of turns of the coil, and the current input to the coil, respectively [25]. The values of g and N were taken from table 2. For quadrupole magnets, the relationship between the magnetic-field gradient k_Q and the excitation current I was based on the measurements shown in fig. 6. The data points are fitted with the septic function

$$I(k_Q) = C_1 k_Q + C_3 k_Q^3 + C_5 k_Q^5 + C_7 k_Q^7,$$
 (2)

where the parameters for QM11U/D are $C_1 = 41.886 \, \text{A/(kG/cm)}$, $C_3 = -20.176 \, \text{A/(kG/cm)}^3$, $C_5 = 0.3988 \, \text{A/(kG/cm)}^5$, and $C_7 = 3.4532 \, \text{A/(kG/cm)}^7$, and those for QM12U/M/D are $C_1 = 70.619 \, \text{A/(kG/cm)}$, $C_3 = 12.794 \, \text{A/(kG/cm)}^3$, $C_5 = -44.376 \, \text{A/(kG/cm)}^5$, and $C_7 = 40.244 \, \text{A/(kG/cm)}^7$. The overall behavior of experimental excitation currents is well described by the calculations. It is noted that the experimental configuration of QM12U/M/D was opposite to that of the calculations for the combination of $R_{B\rho} = 1$ and $\theta_s = 4.5^\circ$, since it was designed so that either configuration would be viable. Most of the experimental currents for dipole and quadrupole magnets are consistent with the calculations with a few exceptions. For the dipole magnets, the discrepancy was due to the over-simplified estimation of the excitation function of the current, where the fringing field and the saturation of the dipole magnet was not taken into account.

After tuning the currents of all the magnets with the blank target, the $^{197}{\rm Au}$ or $^{208}{\rm Pb}$ target was inserted to

view the beam spot with the beam viewers and evaluate the transmission. Table 7 lists the transmission for each setting. It is noted that all the transmissions were less than 97%, while the designed transmission was larger than 99% with the blank targets. This transmission loss was considered to be spurious due to a negative offset of the current readout of the wall beam dump. In fact, when the beam current was increased, the transmission was improved. Therefore, the absolute value of the transmissions in table 7 may contain some uncertainties especially for the low beam intensities, while the relative values with the same intensity should be reasonable. In addition, the readings from the Faraday cup (BS3) at the entrance of the West Experimental Hall had value fluctuations of no more than 0.3 nA, giving an additional uncertainty to the transmission.

3 CAGRA+GR campaign

The CAGRA+GR campaign experiments were performed from October–December 2016 at RCNP. The motivation of this campaign was to study a) the nature of the pygmy dipole resonances, b) isovector spin-flip responses of nuclei for astrophysical neutral-current neutrino-nucleus scattering, c) γ -transitions in the super-deformed band-head, and d) excitation of high-spin states via light-ion reactions.

Figure 7 shows the experimental setup with the CA-GRA and GRAF beamline. The target was surrounded by an array consisting of twelve clovers and four LaBr₃:Ce de-

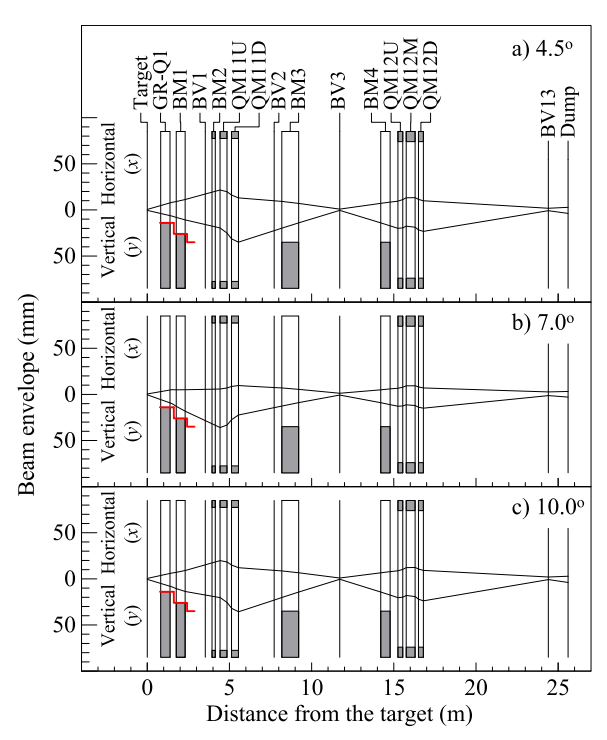


Fig. 4. As in fig. 3, the envelopes of the beam in the horizontal and the vertical directions for $R_{B\rho} = 1$ are shown. The top, middle, and bottom panels correspond to a θ_s of (a) 4.5°, (b) 7.0°, and (c) 10.0°, respectively.

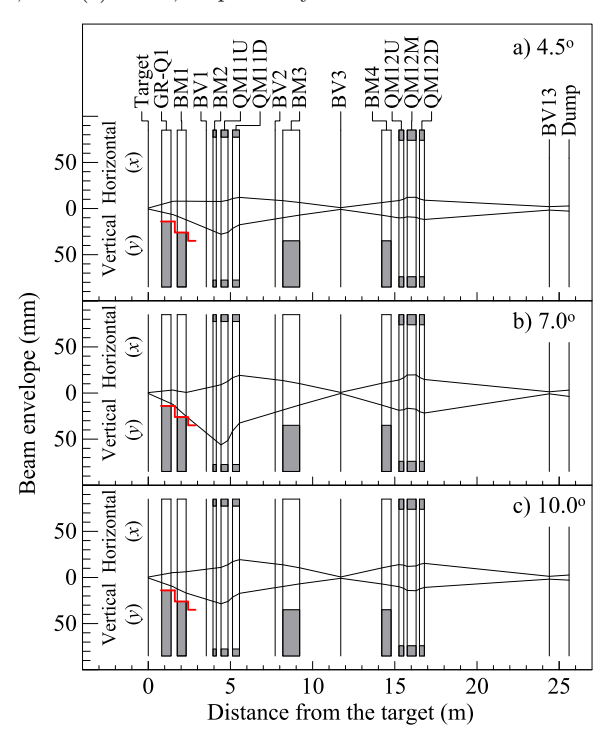


Fig. 5. As in fig. 4, but for $R_{B\rho} = 2$.

tectors. Eight clovers brought from Argonne National Laboratory (ANL) were located at 90°, two clovers from US Army Research Laboratory (ARL) and two clovers from the Institute of Modern Physics (IMP) were positioned

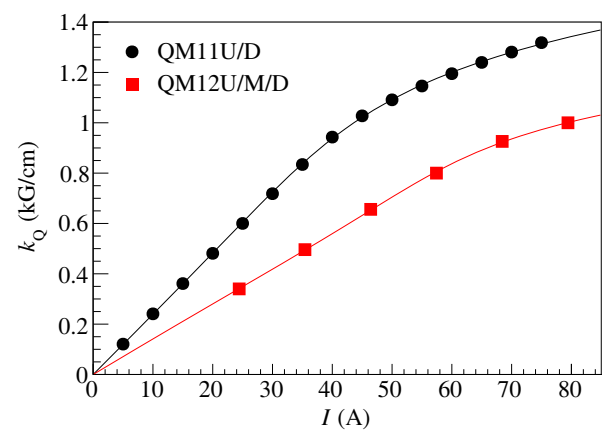


Fig. 6. The data points show the relation between the magnetic gradient k_Q and the excitation current I for the coils of the quadrupole magnets QM11U/D and QM12U/M/D. The curves represent the fit results with the inverse function $I(k_Q)$ described by eq. (2).

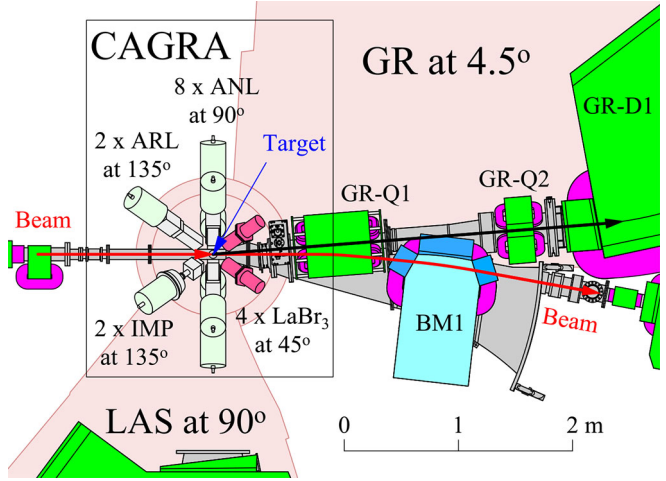


Fig. 7. The experimental setup of the CAGRA+GR campaign with the GRAF beamline is shown. The GR and LAS angles are set to 4.5° and 90° , respectively, in this figure.

at 135° . The distance between the target and the front surface of the housing of the clovers was $205\,\mathrm{mm}$ for the ANL and ARL clovers and $160\,\mathrm{mm}$ for the IMP clovers. BGO Compton-suppression shields from ANL were used for the ANL and ARL clovers. The LaBr₃:Ce detectors were brought from INFN sezione di Milano and installed at 45° . The target was tilted by 22.5° from the direction perpendicular to the beam in order to minimize the material between the target and detectors.

The beam intensity of each measurement was limited by the count rates of the clover crystals. The energy resolution of the clovers deteriorated for higher count rates, and thus the count rates of the individual clover crystals were limited to less than $\sim 20\,\mathrm{kHz}$ for the ANL and ARL clovers and $\sim 40\,\mathrm{kHz}$ for the IMP clovers throughout the campaign. The typical count rates for the individual clover crystals are listed in table 8. The 80 MeV proton, $130\,\mathrm{MeV}$ α , and $600\,\mathrm{MeV}$ $^6\mathrm{Li}$ beams impinged on the named targets in the GRAF mode, and the $295\,\mathrm{MeV}$ proton and $600\,\mathrm{MeV}$ $^6\mathrm{Li}$ beams hit the named targets in

Table 8. Typical count rates of each single crystal used in the CAGRA+GR campaign are shown for each clover, target, beam particle and energy. θ_{clover} represents the angle of the clover with respect to the direction of the beam. The count rate for the 0° inel. mode is shown and the GRAF mode for comparison. Only the $R_{B\rho} = 1$ setting was used in this campaign. The trigger rate and live time of the GR DAQ are also shown.

Mode	Beam particle	Target	Beam		Cour	nt rate (kHz)	θ_s	GR	DAQ
	and energy		intensity	$\theta_{ m clover}$	90°	135°	135°	=	trigger	live
			(enA)	type	ANL	ARL	IMP		rate (kHz)	$_{ m time}$
GRAF	Proton 80 MeV	$^{90}{\rm Zr}~1.95{\rm mg/cm^2}$	7.5		12	10	21	6.6°	0.53	99%
		$^{94}{ m Zr}~4.0{ m mg/cm^2}$	3.7		12	10	21	6.6°	0.52	99%
		$^{124}{ m Sn}~4.0{ m mg/cm^2}$	3.9		12	10	21	6.6°	0.62	98%
		206 Pb 1.3mg/cm^2	13		14	12	23	6.6°	1.1	97%
		208 Pb $2.03\mathrm{mg/cm^2}$	15		18	16	29	4.5°	4.0	93%
	$\alpha~130\mathrm{MeV}$	$^{\rm nat}{ m Si}~11{ m mg/cm}^2$	2.6		19	15	33	9.1°	1.2	96%
		64 Ni $3.55\mathrm{mg/cm^2}$	9.2		22	17	37	4.5°	0.51	99%
		$^{90}{\rm Zr}~1.95{\rm mg/cm^2}$	10		18	14	31	4.5°	0.50	99%
		94 Zr 4.0mg/cm^2	5.8		20	16	34	4.5°	2.9	94%
		120 Sn $2.7 \mathrm{mg/cm^2}$	4.8		17	14	30	4.5°	3.0	93%
		206 Pb $1.3 \mathrm{mg/cm^2}$	14		16	12	27	4.5°	2.9	93%
	$^6\mathrm{Li}~130\mathrm{MeV}$	40 Ca $1.6 \mathrm{mg/cm^2}$	8.0		7.2	6.5	14	11.2°	0.52	99%
		100 Mo $2.0 \mathrm{mg/cm^2}$	8.8		16	15	29	11.2°	0.60	99%
	$^6\mathrm{Li}~600\mathrm{MeV}$	40 Ca $1.6 \mathrm{mg/cm^2}$	10		11	7.3	16	11.2°	0.65	95%
		100 Mo $2.0\mathrm{mg/cm^2}$	10		21	16	31	11.2°	0.46	95%
0° inel.	Proton 295 MeV	blank	2.5		6.9	8.3	10	0.0°	0.54	97%
		64 Ni $3.55\mathrm{mg/cm^2}$	2.4		12	12	18	0.0°	2.8	95%
	$^6\mathrm{Li}~600\mathrm{MeV}$	24 Mg 9.8 mg/cm 2	0.31		3.8	2.7	5.7	0.0°	6.1	89%
		56 Fe $9.47 \mathrm{mg/cm^2}$	1.1		10	8.1	16	0.0°	7.8	87%
		93 Nb 10.9mg/cm^2	1.1		13	12	22	0.0°	6.8	89%

the 0° inelastic-scattering mode as shown in table 8. While the crystals of the ANL and ARL clovers had the same volume, those of the IMP clovers had a larger volume than the ANL and ARL clovers, which allowed for the higher count rates of the IMP clovers.

Figure 8 shows an example of the coincidence matrix between the excitation energy E_x obtained by the GR spectrometer and the deexcitation γ -ray energy E_{γ} detected by the CAGRA clovers for the reaction $^{208}\text{Pb}(p,p'\gamma)$ at $E_p=80\,\text{MeV}$ and $\theta_s=11.2^\circ$. The diagonal line corresponding to direct decay to the g.s. is clearly seen with the single and double escape peaks up to the neutron threshold $S_n=7.36787(5)\,\text{MeV}$ [26]. Another line situated 2.6 MeV below the diagonal line corresponds to the γ decay through the first 3⁻ state of ^{208}Pb . By using the GRAF and 0° inelastic-scattering modes, it became possible to perform measurements with high beam intensities resulting in higher statistical certainties.

The first results of this campaign were published by Sullivan et al. [27]. The physical aim of this study was to provide inelastic neutrino-nucleus scattering cross sections for the understanding of core-collapse supernovae and of the detection processes of emitted neutrinos from such events in earth-based detectors. Furthermore, this study aimed to develop indirect techniques using the (^6Li , $^6\text{Li}*[T=1,\ T_z=0,\ 0^+,\ 3.65\,\text{MeV}]$) reaction at $100\,\text{MeV/u}$ as a probe for isolating the isovector spin-

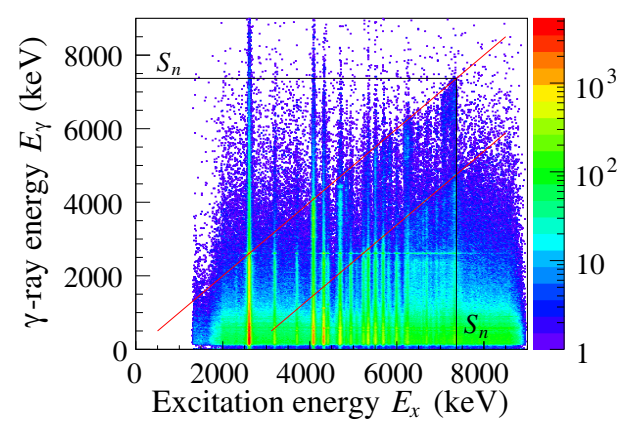


Fig. 8. The coincidence matrix between the excitation energy E_x of ^{208}Pb and deexcitation γ -ray energy E_γ detected by clover detectors is shown. Random coincidences have not been subtracted in this figure.

transfer excitations in the inelastic channel ($\Delta S=1$, $\Delta T=1$, $\Delta T_z=0$). From the excitation cross sections, the Gamow-Teller transition strengths relevant to the inelastic neutrino-nucleus scattering cross sections were extracted. In the experimental setup, the clover detectors were utilized to select events involving the 3.56 MeV γ ray from the decay of the ⁶Li*[3.56 MeV] state.

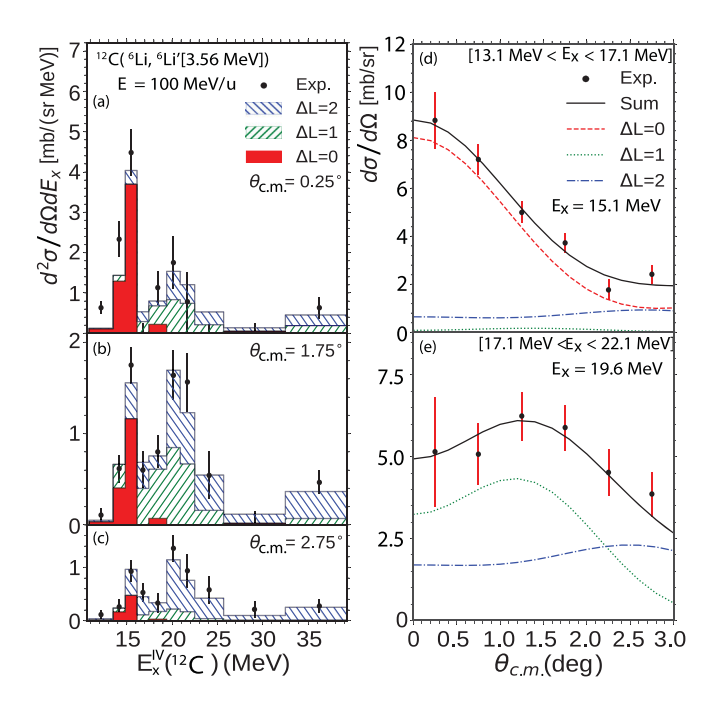


Fig. 9. Double-differential cross sections at (a) 0.5° , (b) 1.75° , and (c) 2.75° for the $^{12}\text{C}(^{6}\text{Li}, ^{6}\text{Li}^{*}[3.65\,\text{MeV}])$ reaction are shown. Examples of the multipole-decomposition analysis (MDA) in the differential cross sections for excitation-energy ranges of (d) $13.1\text{--}17.1\,\text{MeV}$ and (e) $17.1\text{--}22.1\,\text{MeV}$ are presented. The theoretical calculations for $\Delta L = 0$, 1, and 2 were performed in the distorted-wave Born approximation (DWBA). The figure was taken from ref. [27].

For the $^{12}\mathrm{C}(^6\mathrm{Li},^6\mathrm{Li}^*[3.65\,\mathrm{MeV}])$ reaction, the isovector spin-transfer excitation-energy spectrum in the inelastic channel was successfully measured as shown in fig. 9. Thus it was demonstrated that the ($^6\mathrm{Li},^6\mathrm{Li}^*[3.65\,\mathrm{MeV}]$) reaction can be used to isolate the inelastic isovector spin-transfer response. In the cases of $^{24}\mathrm{Mg}$ and $^{93}\mathrm{Nb}$, the 3.56 MeV γ -ray peak could not be isolated from the strong background in the γ spectrum due to the decay of the isoscalar excitations. It is suggested that applications involving nuclei with mass numbers of about 25 or more will require a more efficient γ -ray detector array with a better tracking capability. The data analysis for other experiments of the CAGRA+GR campaign is ongoing.

4 GR+SC γ LLA experiment

The scintillation γ -ray detector array, SC γ LLA, was constructed from the large volume LaBr₃:Ce detectors [20] and a pilot experiment for a coincidence measurement of the γ decay of giant resonances to the g.s. was performed in July 2018. SC γ LLA consists of four detectors at 90° and four detectors at 135°. The side view of the experimental setup is shown in fig. 10. The distance from the target to the surface of the detector was adjustable and set to 137 mm at 90° and 135 mm at 135°. The target inside the chamber was tilted by 22.5° from the direction

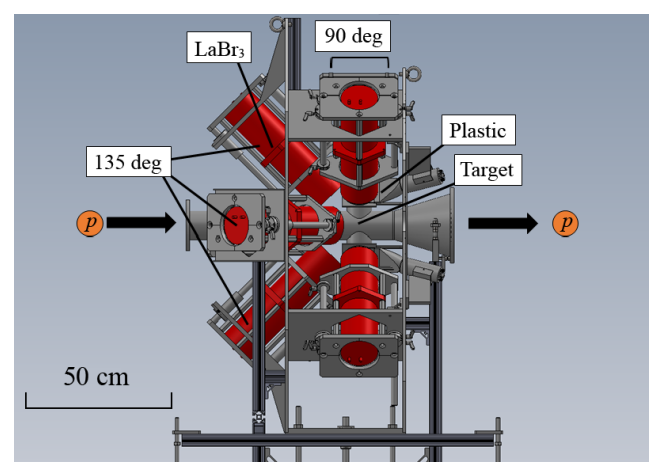


Fig. 10. The side view of the $\gamma\text{-ray}$ detector array SC γLLA is shown.

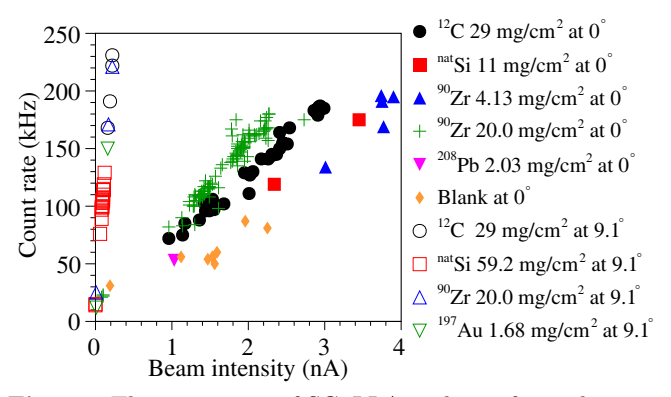


Fig. 11. The count rate of SC γ LLA is shown for each target, beam intensity, and GR angle θ_s . The detector of slot #1 at 90° is selected to show the rate in this figure. Count rates of other detectors indicate a similar tendency. The proton beam at 392 MeV was stopped in the 0° beam dump for the measurement at 0° and was stopped by the Q1-FC without using the GRAF beamline for the measurement at 9.1° .

perpendicular to the beam. The solid angle coverage of the array was around 20% of 4π . In order to eliminate the background events due to charged particles, four veto plastic scintillators with a thickness of 2 mm were placed in front of the 90° detectors. Lead absorbers with thicknesses of 2 mm and copper absorbers with thicknesses of 4 mm were inserted in front of the veto scintillators at 90° and in front of the LaBr₃ detectors at 135° to reduce the atomic background level from the target.

The maximum beam intensity of each measurement was limited by the detector count rates similarly to in the CAGRA+GR campaign. The detectors here, however, had a better rate-capability. Figure 11 shows the count rate of a detector at 90° as a function of the proton beam intensity at 392 MeV for each target. Each data point corresponds to each run taken in the experiment. The data points with open symbols represent the measurements where the GR angle θ_s was set to 9.1° and the beam was stopped in the Faraday cup, Q1-FC, located downstream from the GR-Q1, without using the GRAF beamline. The other data points represent the count rates for the 0°

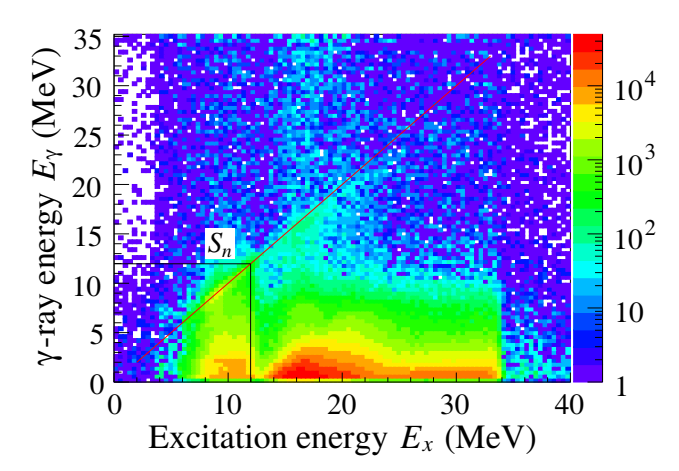


Fig. 12. The coincidence matrix of E_x vs. E_{γ} for the $^{90}\text{Zr}(p,p'\gamma)$ reaction at $E_p=392\,\text{MeV}$ is shown. The direct decay to the ground state is clearly seen in the diagonal line.

inelastic-scattering mode. The count rates largely depend on the distance between the detectors and the beam stop position, where intense radiation is produced. Even in the 0° inelastic scattering setup with the blank target, the neutron radiation from the 0° beam dump caused large random coincidence events in the count rates of the detectors. The location of the Q1-FC in the 9.1° setup is much closer to the detectors than the 0° beam dump, and thus the radiation from the Q1-FC increased the count rates.

The experimental data were properly taken by the standard DAQ of GR. Figure 12 shows the coincidence matrix of the excitation energy E_x and the deexcitation γ -ray energy E_{γ} for the $^{90}{\rm Zr}(p,p'\gamma)$ reaction. The direct decay to the g.s. is seen in the diagonal line below and above the $S_n=11.968(3)$ MeV. The analysis of the branching ratio of the particle decay to the γ decay is ongoing.

5 Summary and outlook

Electric dipole excitation is one of the fundamental excitation modes in atomic nuclei. Extensive studies on the pygmy dipole resonances and isovector giant dipole resonances have been performed in recent years. In this article, we discussed the importance of the coincidence measurements between the excitation and γ -decay processes, while in most cases, γ decays have been measured without tagging the excitation process (see e.g. real photon measurements in [4,5]) or only the excitation process was detected [8]. We presented two experimental setups: the 0° inelastic-scattering mode and the GRAF mode. The GRAF beamline has been newly constructed at RCNP and has significantly improved the experimental feasibility of coincidence measurements by placing the GR spectrometer at forward angles with relatively intense primary beams. Details of the technical design of the GRAF beamline as well as its commissioning process were described.

We presented two example cases of γ -decay coincidence measurements. They were performed with a clover ger-

manium detector array (CAGRA) at finite angles and a $LaBr_3$ scintillation detector array (SC γ LLA) at 0°. Experimental conditions and coincidence matrices are presented in this article, and the data analysis will be finalized in the near future. These successful technical developments will drive future experimental studies on the structure of the excitation modes in atomic nuclei. We note that an experimental campaign using the GR+SC γ LLA setup is planned at RCNP and beam-time proposals for the campaign are being collected.

We are grateful to N. Blasi, A. Bracco, F. Camera, F. Crespi, and O. Wieland at INFN sezione di Milano for collaborating on the LaBr₃:Ce detectors and to S. Zhu at ANL, J.J. Carroll at ARL, and Y.D. Fang and X.H. Zhou at IMP for collaborating on the CAGRA clover detectors. We thank G. Gey for the early development of the CAGRA+GR campaign and K. Nagayama, H.P. Yoshida, and M. Uraki for the construction of the GRAF beamline and the CAGRA+GR frame. We acknowledge Y. Fujioka, Y.N. Watanabe, and A. Sakaue for their contribution to the development of the GRAF beamline. We also thank all the collaborators of the CAGRA+GR campaign and the GR+SC γ LLA experiment for realizing the coincidence measurements and the RCNP accelerator staff for the beam delivery during the long beam time. This work was partially supported by the JSPS KAKENHI, under Grant Numbers JP18K13566 and JP14740154, the MEXT KAKENHI, under Grant Number JP25105509, and the U.S. Department of Energy, Office of Science, Office of Nuclear Physics, under Contract No. DE-AC02-06CH11357.

Data Availability Statement This manuscript has no associated data or the data will not be deposited. [Authors' comment: All data generated during this study are contained in this published article.]

Publisher's Note The EPJ Publishers remain neutral with regard to jurisdictional claims in published maps and institutional affiliations.

References

- P.F. Bortignon, A. Bracco, R.A. Broglia, Giant Resonances, Nuclear Structure at Finite Temperature (Harwood Academic Publishers, Amsterdam, 1998).
- M.N. Harakeh, A. von der Wood, Giant Resonances: Fundamental High-Frequency Modes of Nuclear Excitation (Oxford University Press, New York, 2001).
- S. Ebata, T. Nakatsukasa, T. Inakura, Phys. Rev. C 90, 024303 (2014).
- D. Savran, T. Aumann, A. Zilges, Prog. Part. Nucl. Phys. 70, 210 (2013).
- A. Bracco, E.G. Lanza, A. Tamii, Prog. Part. Nucl. Phys. 106, 360 (2019).

- 6. A.M. Krumbholtz et al., Phys. Lett. B 744, 7 (2015).
- A. Tamii et al., Nucl. Instrum. Methods Phys. Res. A 605, 326 (2009).
- P. von Neumann-Cosel, A. Tamii, Eur. Phys. J. A 55, 110 (2019).
- M. Fujiwara *et al.*, Nucl. Instrum. Methods Phys. Res. A 422, 484 (1999).
- M. Brenna, G. Colò, P.F. Bortignon, Phys. Rev. C 85, 014305 (2012).
- 11. J.R. Beene et al., Phys. Rev. C 41, 920 (1990).
- 12. U. Garg, G. Colò, Prog. Part. Nucl. Phys. 101, 55 (2018).
- Y. Fujita, B. Rubio, W. Gelletly, Prog. Part. Nucl. Phys. 66, 549 (2011).
- 14. S. Noji et al., Phys. Rev. Lett. 112, 252501 (2014).
- 15. S. Noji et al., Phys. Rev. C 92, 024312 (2015).
- 16. D. Frekers, M. Alanssari, Eur. Phys. J. A 54, 177 (2018).

- M.N. Harakeh et al., Proceedings of the International Symposuim on New Facet of Spin Giant Resonances in Nuclei (SGR97), 1997, edited by H. Sakai, H. Okamura, T. Wakasa (World Scientific, Singapore, 1998) p. 247.
- 18. M.S. Reen et al., Phys. Rev. C 100, 024615 (2019).
- 19. E. Ideguchi et al., in preparation.
- A. Giaz *et al.*, Nucl. Instrum. Methods Phys. Res. A **729**, 910 (2013).
- 21. S. Terashima et al., Phys. Rev. Lett. 121, 242501 (2018).
- 22. Y.N. Watanabe, PhD Thesis, University of Tokyo (2019).
- 23. N. Matsuoka et al., RCNP Annual Report (1991) p. 186.
- 24. T. Wakasa et al., Prog. Part. Nucl. Phys. 96, 32 (2017).
- 25. S. Humphries jr., *Principles of Charged Particle Acceleration* (John M. Wiley & Sons, Inc., New York, 1986).
- 26. M. Wang et al., Chin. Phys. C 36, 1603 (2012).
- 27. C. Sullivan et al., Phys. Rev. C 98, 015804 (2018).